Research Article

Photocatalytic Degradation of Methyl Green Dye Mediated by Pure and Mn-Doped Zinc Oxide Nanoparticles under Solar Light Irradiation

Rizwan Akram,[1] **Adeena Fatima,**[2] **Ziyad M. Almohaimeed,**[1] **Zahid Farooq,**[3] **Karwan Wasman Qadir** ⓘ**,**[4,5] **and Qayyum Zafar** ⓘ[2]

[1]*Department of Electrical Engineering, College of Engineering, Qassim University, P.O. Box 6677, Buraydah 51452, Saudi Arabia*
[2]*Department of Physics, University of Management and Technology, 54000 Lahore, Pakistan*
[3]*Department of Physics, Division of Science and Technology, University of Education, Lahore 54000, Pakistan*
[4]*Computation Nanotechnology Research Lab (CNRL), Department of Physics, College of Education, Salahaddin University-Erbil, 44002 Erbil, Kurdistan Region, Iraq*
[5]*Renewable Energy Technology Department, Erbil Technology College, Erbil Polytechnic University, 44001 Erbil, Kurdistan Region, Iraq*

Correspondence should be addressed to Qayyum Zafar; qayyumzafar@gmail.com

Herein this study, pure and manganese- (Mn-) doped ZnO (2 wt. %) nanoparticles have been synthesized using the chemical precipitation method and characterized for the photodegradation of methyl green (MG) pollutant dye under natural sunlight. The structural analysis via XRD patterns has revealed that both intrinsic and Mn-doped ZnO (2 wt. %) samples have hexagonal wurtzite structures with appropriate phase purity, clearly indicating the absence of any external impurity. The incorporation of Mn in the host ZnO lattice has decreased the crystallite size ($21.10 \rightarrow 18.76$ nm), and nanoparticle-type surface features with sizes in the 50–100 nm range have been observed through FESEM-based surface morphological studies. Both aforementioned observations have merit in providing more active area and a high surface area to volume ratio for photocatalytic reaction. The investigation of photophysical properties indicates that in Mn-doped ZnO nanoparticles, the absorption peak is blue-shifted by 5 nm ($365 \rightarrow 360$ nm), due to the widening of the bandgap. The degradation kinetics of MG dye follow the pseudo-second-order kinetics, and the degradation efficiency has been observed to be 62.78% mediated by pure ZnO and 66.44% by Mn-doped ZnO (2 wt. %) photocatalyst under 60 minutes of sunlight irradiation. Specifically, the rate of photocatalytic reaction (K) ~ 0.01792 min^{-1} and $R^2 \sim 0.97992$ has been achieved for pure ZnO, whereas slightly higher (K) ~ 0.02072 min^{-1} and $R^2 \sim 0.97299$ have been observed for Mn-doped ZnO, respectively. Conclusively, the synergistic interactions with multiple charge transfer pathways, improvement of e$^-$/h$^+$ pair charge separation, improved surface area, and efficient generation of hydroxyl radicals are supposed to be responsible for the highly efficient photocatalytic activity of the Mn–doped ZnO photocatalyst for MG dye.

1. Introduction

Water pollution as a consequence of rapid industrial development, urbanization, and the bulging human population has become the most decisive and challenging environmental problem across the globe [1, 2]. In particular, the exten-sive discharge of untreated organic dyes from the leather, textile, and apparel industries is rapidly contaminating the already dwindling water resources [3, 4]. Distressingly, these synthetic dyes are intrinsically chemically and physically stable compounds; hence, based on their stability and solubility in water, synthetic dyes (if not treated) pile up in industrial

effluents and wastewater [5]. Rationally, there exists a dire need for the development of highly efficient, economical, easily accessible, eco benign, and sustainable green solutions (based on a renewable energy approach) to mitigate the water pollution crisis.

In the recent past, various research strategies/technologies have been adopted for the remediation of industrial wastewater and dye-contaminated water bodies, including plasma-based advanced oxidation process [6], ozonation [7], membrane filtration [8], bioelectrochemical system [9], heterogeneous Fenton catalysts [10], ion exchange removal [11], adsorption, and electrocoagulation [12]. Among these, the photocatalysis process mediated by metal oxide semiconductors is an environmentally safe process that simulates the natural photosynthesis process to speed up the chemical reactions requiring light [13]. In particular, the countries where ample amount of sunlight is available, photocatalysis involving sunlight may prove to be the most economical and desirable process. Further, photocatalytic degradation offers benefits over traditional wastewater treatment methods in terms of high effectivity, cost-effectiveness, and energy efficiency [14]. In literature, various synthetic routes have been proposed, such as hydrothermal [15] and metal-organic chemical vapor deposition method (MOCVD) [16] for the synthesis of metal oxide photocatalysts.

Among the numerous metal oxide semiconductors, TiO_2 and ZnO are known to be exceptional photocatalysts due to their notably high photosensitivity, nontoxic nature, and wide bandgap (WBG) [17]. However, ZnO is anticipated to be an appropriate substitute for TiO_2 due to its similar bandgap energy, lower cost, and effective capability to degrade organic pollutants in aqueous solutions [18]. ZnO nanoparticles absorb more light photons than TiO_2 nanoparticles under the same ambient conditions [19]. ZnO is a versatile inorganic compound with distinctive physicochemical and optoelectronic properties such as high electron mobility, large exciton binding energy, greater chemical and thermal stability, and strong oxidation capability [20, 21]. Recently nanosized ZnO particles have received considerable attention in photocatalytic applications due to high specific surface area and low-cost production possibility [22]. However, ZnO exhibits high recombination of photogenerated electron-hole pairs. One effective route to reduce the recombination rate is by doping the ZnO with transition-metal cations, which creates traps that immobilize the charge carriers and thus reduce the recombination rate [23]. Manganese is considered one of the best dopant materials because of its high solubility, abundant electron states, and large magnetic moment [24]. Successful doping of ZnO with manganese (Mn) has been previously reported to cause a hyperchromic shift in the optical absorption of ZnO, which may be attributed to the shrinkage of the native optical bandgap of ZnO [25]. Ruh Ullah and Dutta have previously experimentally demonstrated that coupling of ZnO with Mn (ZnO : Mn^{2+}) leads to improved photodegradation towards methylene blue dye owing to a substantial increase in defect sites caused by Mn^{2+} doping [26].

In our previous study, we described an effective route for the degradation of methyl green (MG) dye under visible light illumination by pristine- and strontium- (Sr-) doped zinc oxide (ZnO) photocatalysts [27]. So far, to reduce the recombination rate, most of the R&D efforts have been directed at narrowing the bandgap of photocatalysts by introducing dopant(s) into the structure of the host semiconductor and resultantly harvesting visible instead of UV light [28]. Improving the photocatalytic activity of WBG photocatalysts, without sacrificing the high bandgap energy, may also improve the disinfection process by UV light and further reduce operating costs by process intensification [29].

2. Experimental Procedures

2.1. Chemical Reagents. For the synthesis of pure and Mn-doped ZnO nanoparticles, the chemical precipitation synthesis route has been adopted. The chemicals used in the present study were all analytical-grade reagents and were used without further refinement. For instance, the zinc and manganese precursors, i.e., zinc nitrate hexahydrate (molar mass = 297.46 g/mol, $Zn(NO_3)_2.6H_2O$) and manganese (II) nitrate (molar mass = 178.95 g/mol, $Mn(NO_3)_2$), respectively, have been purchased from Duksan, Korea. The precipitating agent, 98% pure sodium hydroxide pellets (molar mass = 40 g/mol, NaOH), has been purchased from Sigma-Aldrich. In the present study, all the aqueous solutions have been prepared in deionized (DI) water. Methyl green dye (molar mass: 653.24 g/mol, $C_{27}H_{35}Cl_2N_3.ZnCl_2$) has been subjected to photocatalytic degradation mediated by pure and Mn-doped zinc oxide photocatalysts, in this study.

2.2. Synthesis of Pure and Mn-Doped ZnO. In this chemical synthesis procedure, one molar (1 M) $Zn(NO_3)_2.6H_2O$ solution has been prepared in deionized water and subjected to vigorous stirring (for one hour) by placing it on a hot plate (T ~100°C). Later, the base solution, i.e., unimolar NaOH aqueous solution, has been prepared, under gentle magnetic stirring for 30 mins at room temperature, to obtain a homogenous alkaline solution. The precipitating agent, i.e., NaOH solution, has been gradually (dropwise) introduced into zinc nitrate solution, accompanied by constant magnetic stirring, until the alkalinity of the solution increases significantly (specifically, pH reaches 12). At this stage, the white milky suspension is achieved, wherein the precipitates are allowed to settle down, and the supernatant solution is decanted, carefully. The white precipitates, so obtained, have been washed (five times) with deionized water to remove impurities, if any. Later, the precipitates have been filtered and dried in an oven (overnight, at T ~300°C) to remove the moisture completely. Lastly, the as-prepared ZnO powder (pure) has been finely grounded in a mortar with the help of a pestle to obtain ZnO nanostructures. The synthesis procedure (adopted in the present study) for pure and metal-doped ZnO nanoparticles is well-reported in the literature [30, 31].

For the preparation of Mn-doped ZnO nanostructures, the same aforementioned synthesis procedure has been followed, except for the further addition of manganese precursor, i.e., 2 wt. % manganese nitrate in zinc nitrate
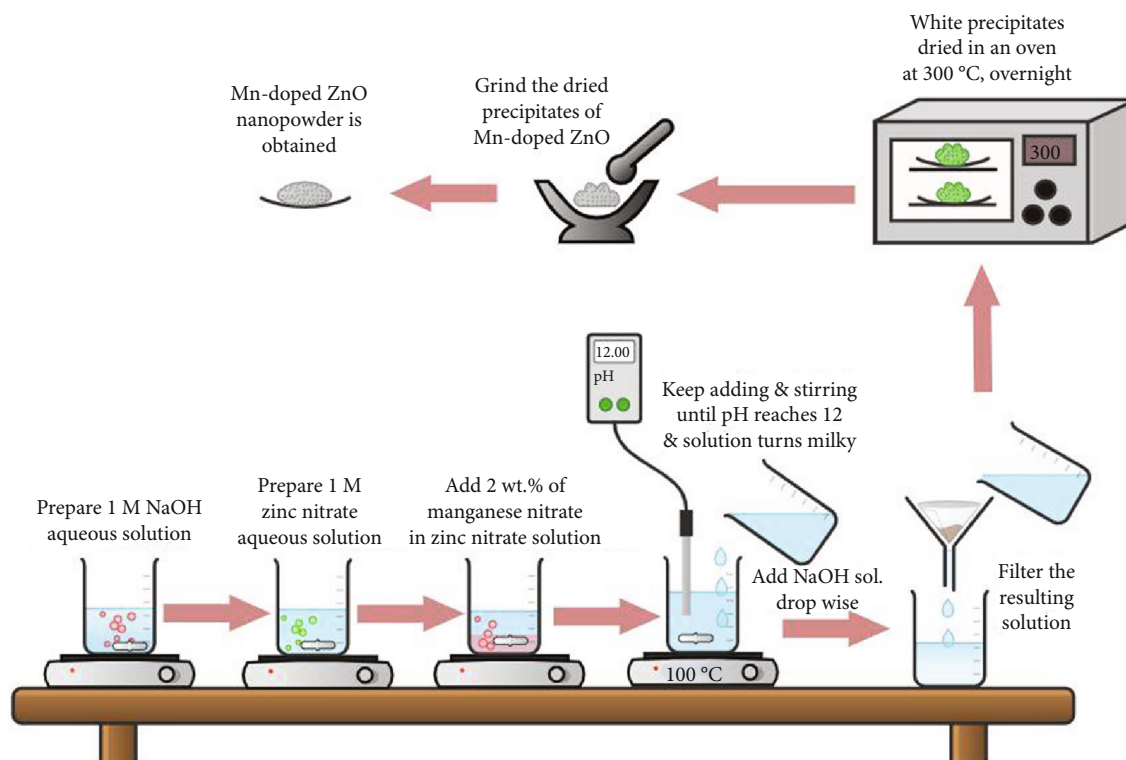
Figure 1: The synthesis route of Mn-doped ZnO nanoparticles via the chemical precipitation method.

solution. Figure 1 summarizes (in pictorial form) the procedure adopted for the synthesis of Mn-doped ZnO photocatalyst.

2.3. Photocatalytic Activity. Herein this study, we have investigated the photocatalytic activity (PCA) of pure and Mn-doped ZnO nanoparticles for the effective degradation application of MG dye under natural sunlight irradiation. The MG dye has been specifically selected as a model dye for our investigation, on account of its extensive discharge as an industrial effluent coupled with its adverse effects on human health. The MG dicationic dye exhibits peak absorbance in the visible range, specifically at $\lambda_{max} = 620$ nm. To perform the PCA, primarily 2 mg MG dye has been dissolved in 100 mL of deionized water (DIW) with persistent stirring via a magnetic stirrer. Secondly, 3 mg of both synthesized photocatalysts (pure and Mn-doped ZnO) has been sequentially dispersed in 30 mL aliquots of MG aqueous solution. To achieve adsorption saturation between the photocatalyst and dye solution, their dispersion has been vigorously stirred, in dark conditions, for half an hour. No substantial evidence of MG dye degradation mediated by synthesized photocatalysts was observed in the dark condition. It is pertinent to mention that we have selected the catalyst dosage and MG dye concentration after optimization through the UV-visible spectrophotometer. Still, higher concentrations would hamper light transmission through the aqueous dispersion in the optical study via UV-vis spectrophotometer.

The vials containing MG dye and the synthesized photocatalysts were later sequentially irradiated with sunlight under constant stirring, per 10 minute time intervals for about an hour. The reaction mixture has been irradiated by natural sunlight, specifically between the hours of 11 a.m. and 12 p.m. on a bright sunny day (27th September 2021, Lahore, Pakistan), where variation in sunlight intensity was monitored to be nearly minimum. As it is well understood that society has become increasingly conscious of the adverse impacts of rapid industrial development on the global ecosystem and resultantly, sustainable development has become a popular catchphrase, recently. In general, the UV light used in photocatalysis requires an input of energy for its generation, which increases both the cost and environmental footprint of the processes as compared to nonpolluting and renewable natural sunlight [32]. Contrariwise, in tropical countries, ample sunlight is readily available throughout the year; therefore, using natural sunlight as a light source is the logically more promising and sustainable approach which may add substantially to the economic and practicability of the photocatalytic process to meet the actual needs of water decontamination [33].

The progress of photocatalytic decolorization of MG dye has been experimentally monitored by extracting 3 mL of analytical samples, each after 10 min intervals. Chiefly, after photodegradation and decolorization, the characteristic dark green color of the MG dye aqueous medium was observed to fade away and, in the long run, turned pale green as the irradiation period progressively increased. Specifically, in our study, the quantification of photocatalytic degradation of MG dye has been achieved via UV-vis spectroscopy in the near UV-visible wavelength range of 300-800 nm, wherein the concentration of dye is estimated by registering the
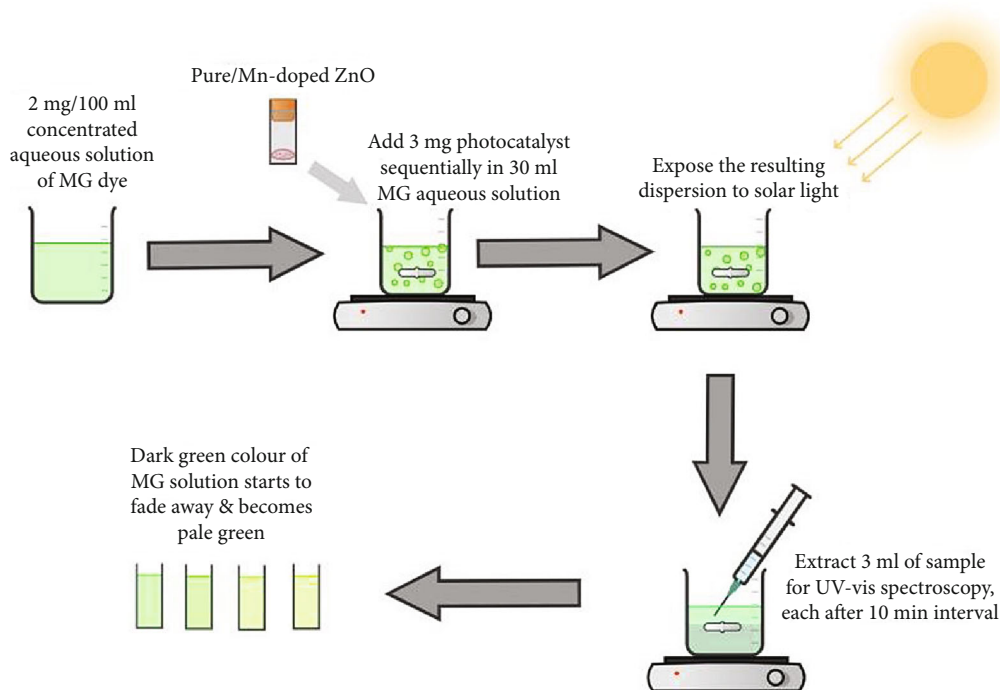
FIGURE 2: Photocatalytic activity of pure and Mn-doped ZnO towards methyl green (MG) dye, under natural sunlight irradiation.

absorption spectrum of its aqueous solution. Figure 2 displays a pictorial rendition of the photocatalytic activity of (a) pure ZnO and (b) Mn-doped ZnO towards MG dye. The degradation efficiency has been determined by the following mathematical expression [34]:

$$\text{Degradation Efficiency} = \left(\frac{C_o - C_t}{C_o}\right) \times 100(\%), \qquad (1)$$

where C_o represents the initial concentration of MG aqueous solution under dark conditions and C_t represents the concentration at varied time intervals under natural sunlight irradiation conditions.

The absorption spectrum of the pure and Mn-doped nanostructures has been examined by AE-S60-2U UV-vis spectrophotometer (A & E Lab Instruments, Guangzhou, China). The UV-vis measurement has been accomplished after the rigorous dispersion of metal oxide nanoparticles in deionized water. The surface morphology of the pure and Mn-doped ZnO (2 wt. %) nanoparticles has been studied by a high-resolution Nova Nano-450 field emission scanning electron microscope (FESEM). The XRD patterns of the synthesized photocatalysts have been recorded using D-8 Discover (Bruker, Germany). The structural characterization of pure and Mn-doped ZnO has been performed by XRD over the range between 20° and 80° with the diffractometer functioning of Cu Kα1 radiations ($\lambda = 0.15406$ nm) generated at 40 kV voltage and a current of 40 mA and the repetition rate of 2° min^{-1}.

3. Results and Discussion

To study the structural properties, phase purity, and crystallite size estimation, the X-ray diffraction patterns of pure and Mn-doped (2 wt. %) ZnO nanoparticles have been examined in the range of $2\theta = 20 - 80°$, as shown in Figure 3(a). It may be observed that sharp peaks appear at about $2\theta = 31.92°$ corresponding to the (100) plane, 34.60° (002), 36.40° (101), 47.68° (102), 56.61° (110), 62.92° (103), 66.56° (200), 67.97° (112), and 69.10° (201), which are envisaged to be characteristic peaks of ZnO crystalline structure [35]. Specifically, the identified peaks for all planes are in strong agreement with the standard peak positions of the ZnO hexagonal wurtzite structure with space group P63mc (JCPDS card no.: 00-036-1451). In general, the XRD diffraction pattern signifies the polycrystalline nature with strongly preferred (101) plane direction of ZnO photocatalyst, synthesized via chemical precipitation route. Notably, no crystalline by-products such as manganese, manganese oxide, or mixed manganese-zinc oxide have been observed, which further confirms the singularity of the hexagonal wurtzite ZnO phase and the successful doping of manganese in the ZnO host lattice. Additionally, the definite line broadening of the XRD peaks may serve as an indirect indication that the synthesized ZnO particles are in the nanoscale range [36]. Furthermore, no significant loss in crystallinity was observed after photocatalysis as evident from Figure 3(a) (inset).

The synthesis of semiconductor materials with controlled doping is a tedious task since either the doping ions are found segregated at nanocrystal surfaces or they even
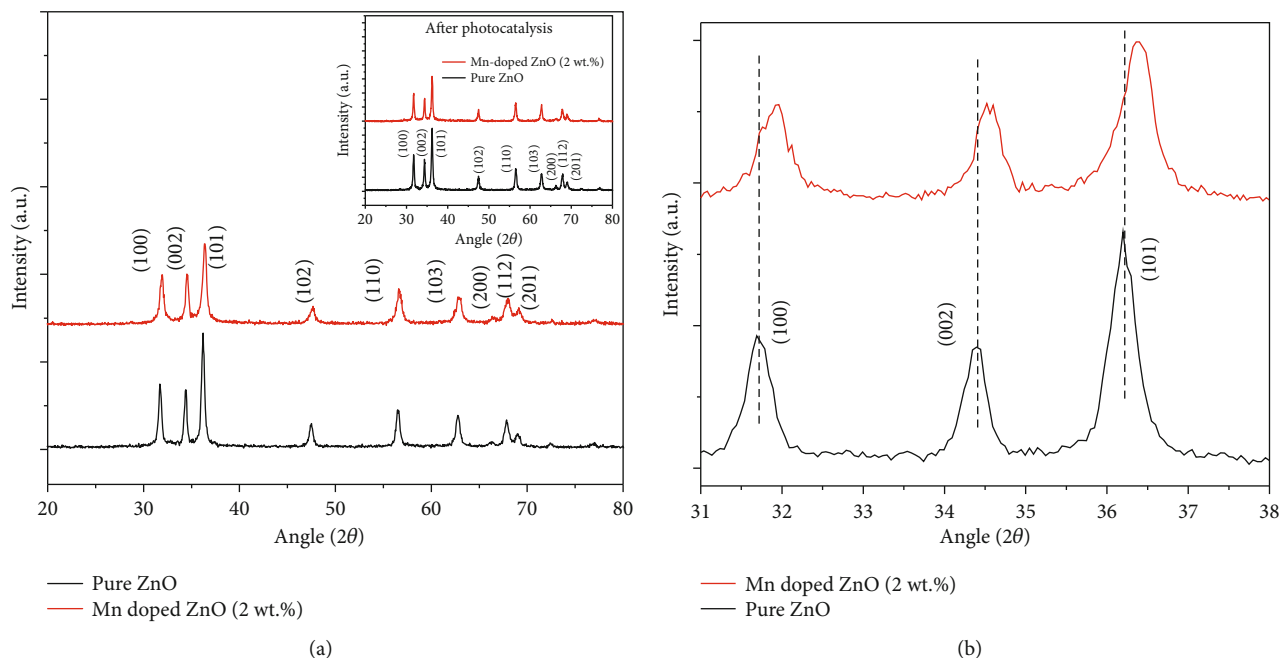
FIGURE 3: (a) The XRD patterns of pure and Mn-doped (2 wt. %) ZnO nanoparticles before and (inset) after photocatalysis and (b) the relative peak shift towards higher angles with Mn-doping in the ZnO host matrix.

form secondary phases, rather than being incorporated in the core [37]. Albeit, the XRD pattern of the Mn-doped ZnO seems nearly identical to that of the pure ZnO. However, from Figure 3(a), it may be primarily inferred that the diffraction peak intensity has decreased with the doping of Mn^{2+} content in the ZnO matrix. This observation indicates that the dopant ions have substituted the inner lattice of Zn^{2+} ions, as it has caused the crystallinity to degenerate (i.e., lattice disorder) and increase in the concentration of defects in the sample [38–40]. Secondly, interestingly, we have also observed a shift of XRD peaks in the case of Mn-doped ZnO towards higher 2θ values compared to those of pure ZnO. Specifically, Figure 3(b) demonstrates a slight shift in the center of the three most intense (100), (002), and (101) diffraction peaks observed for the Mn-doped ZnO nanostructures. This interesting observation indicates that Mn has been successfully incorporated into the host Zn^{2+} lattice sites. The ionic radius of the substitute Mn^{2+} (~0.80 Å) is slightly higher than that of Zn^{2+} (~0.74 Å) [41], so a slender shift towards lower angles was expected indicating the increase of the lattice parameters of the host lattice, as observed in numerous prior studies [39, 42, 43]. In contrast, in various other studies [44–46] and likewise in our present study, it has been experimentally observed that the diffraction peaks have shifted towards higher angles, instead. Shatnawi et al. also observed a decrease in the average crystallite size, and based on the X-ray photoelectron spectroscopy (XPS), results attributed it to the introduction of pronounced lattice defects (oxygen vacancies) with an increase in the Mn-doping level in ZnO [47]. Othman et al. have also observed (a) a shift in diffraction angle towards the higher angles, (b) a decrease in Zn-O bond length, and (c) a decrease in crystallite size with increasing

Mn content in ZnO [48]. This interesting experimental observation may be sourced by the existence of multiple ionization valence states of Mn, such as Mn^{3+} and Mn^{4+} with relatively smaller ionic radii, ca. 0.58 Å, and 0.53 Å, respectively [49].

The X-ray diffractometer (XRD) remains a dominant quantitative analysis tool for the estimation of crystallite size. In general, the Scherrer formula is ubiquitously used to estimate nanostructural parameters, but it only considers the effect of crystallite size on the XRD peak broadening and ignores the important intrinsic strain contribution [50, 51]. Crystallite size and lattice strain measure the size of coherently diffracting domains and the distribution of lattice constants from lattice dislocations, respectively [52]. The origin of the lattice strain is mainly attributed to the point defect, grain boundary, and stacking faults as a result of doping which may ultimately cause lattice expansion or lattice contraction in the nanocrystals [53]. In the present study, the Williamson-Hall (W-H) method has been adopted for the estimation of the crystalline domain size of the synthesized samples, i.e., pure and Mn-doped ZnO. The simplified W-H diagnostic tool assumes that the broadening in Bragg's peaks is the sum of peak broadening due to finite crystallite size and induced strain [54, 55]. The W-H equation is given as [56]

$$\beta \mathrm{Cos}\theta = (K\lambda)/D + 4\varepsilon \mathrm{Sin}\theta, \qquad (2)$$

where "D" is the average crystallite size, K is the shape factor that is equal to 0.9, "λ" is the wavelength of X-rays (1.5406 A˚), "β" is the full width at half of the maximum of diffraction peaks, "θ" is the Bragg's angle, and "ε" represents the internal microstrain.

Table 1: The estimation of crystallite size and microstrain in pure and Mn-doped ZnO samples using the W-H method.

Parameters		Peak position	FWHM	X-axis	Y-axis	Y-intercept	Crystallite size	Microstrain (ϵ)
K	λ(Å)	2θ (deg)	β (deg)	$4\mathrm{Sin}\theta$	$\beta \mathrm{Cos}\theta$		D (nm)	No unit
Structural parameters for pure ZnO XRD's data using Williamson-Hall plot								
0.94	1.5406	36.20237	0.49032	1.242784353	0.008134172	0.00657	21.10410959	0.949×10^{-3}
		34.3841	0.42664	1.182301995	0.007113569			
		31.7238	0.46896	1.093278514	0.007873242			
		47.47716	0.51164	1.61025698	0.008174267			
		56.53489	0.51897	1.89435141	0.007977569			
		62.78453	0.57248	2.083577587	0.008529093			
		67.87294	0.62157	2.233093267	0.009000488			
		68.99383	0.60138	2.265447449	0.008650399			
Structural parameters for Mn-doped ZnO XRD's data using Williamson-Hall plot								
0.94	1.5406	36.36538	0.59023	1.2481916	0.009787068	0.00739	18.7623816	1.5×10^{-3}
		34.54185	0.47705	1.1875614	0.007950683			
		31.90264	0.56533	1.0992822	0.009486951			
		47.60118	0.65403	1.6142189	0.010444196			
		56.66233	0.67434	1.8982682	0.010359701			
		62.88501	0.74308	2.0865708	0.011064849			
		67.96516	0.7939	2.2357633	0.01148964			
		69.10656	0.67618	2.2686894	0.009719761			

The crystallite size of pure and Mn-doped ZnO has been estimated to be ~21.10 nm and 18.76 nm, respectively, as shown in Table 1. It has been observed that the crystallite size of the Mn-doped ZnO sample has decreased as compared to pure ZnO.

Field emission scanning electron microscopy (FESEM) analysis has been conducted to investigate the morphological properties of pure and Mn-doped ZnO nanoparticles. FESEM images have been noted at different magnifications to study the effect of Mn-doping on the shape, size, and distribution of particles. Specifically, FESEM images of both samples at 25,000x and 100,000x magnifications are displayed in Figures 4(a) and 4(b) for pure ZnO and Figures 4(c) and 4(d) for Mn-doped ZnO, respectively. In general, the FESEM micrographs depict nanoparticle-based surface morphology with inhomogeneity in particle size and shapes. However, it may be observed that particles with sizes in the 50–100 nm range are the most frequent in both photocatalysts. The nanoparticle-based surface morphology has merit in providing more surface-to-volume ratio for photocatalytic reaction. Admittedly, the FESEM of the synthesized photocatalysts (in powder form) show aggregation; however, it must be undermined that in the aqueous suspension form during the PCA study, the continuous stirring effectively prevents aggregation and thus maintain a large active surface area of the synthesized photocatalysts.

The light absorption property of the pure and Mn-doped ZnO nanoparticles has also been investigated in the near UV-visible (300–800 nm) wavelength range, as shown in Figure 5. It may be easily observed that both synthesized particles have considerably higher absorption in the UV-A region (300–400 nm) and relatively feeble absorption in the visible range (400–700 nm). Specifically, the pure ZnO nanoparticles exhibit a strong excitonic absorption band at 365 nm, which is envisaged to be the characteristic absorption peak of ZnO nanostructures [57, 58], whereas a slight hypsochromic shift in the absorption peak of the Mn-doped ZnO (~360 nm) is evident as compared to that of pure ZnO nanoparticles. Resultantly, the energy bandgap (E_g) of Mn-doped ZnO nanoparticles (3.4 eV) has increased as compared to that of pure ZnO (3.3 eV), as evidently observed by the Tauc plot depicted in Figure 5 (inset).

Wu et al. have observed similar results, i.e., a blue shift in the absorption edge of ZnO and a broadening of E_g, which indicates that Mn-doping not only produces elemental energy levels but also affects the intrinsic defect energy levels of ZnO [59]. Husain et al. suggest that the blue shift in optical absorption or increase in the E_g, by successive doping of Mn in ZnO, may be attributed to the orbitals hybridized between the Mn atom and host band [60]. Viswanatha et al. also find it reasonable to expect the bandgap (E_g) to increase with increasing concentration of Mn since the bandgap of MnO (E_g~4.2 eV) is greater than that of ZnO (E_g~3.3 eV) [61]. It must be undermined that the crystallite size of as-synthesized ZnO (calculated from XRD) is significantly higher than the Bohr exciton radius of ZnO (i.e., 2.34 nm) [62]; therefore, the increase in bandgap or blue shift in absorption may not be attributed to quantum confinement effect. Instead, similar bandgap widening has been attributed to Burstein-Moss effect which is widely reported (for ZnO) in literature [25, 63, 64]. Nevertheless, based on the efficient absorption of pure and Mn-doped ZnO in the
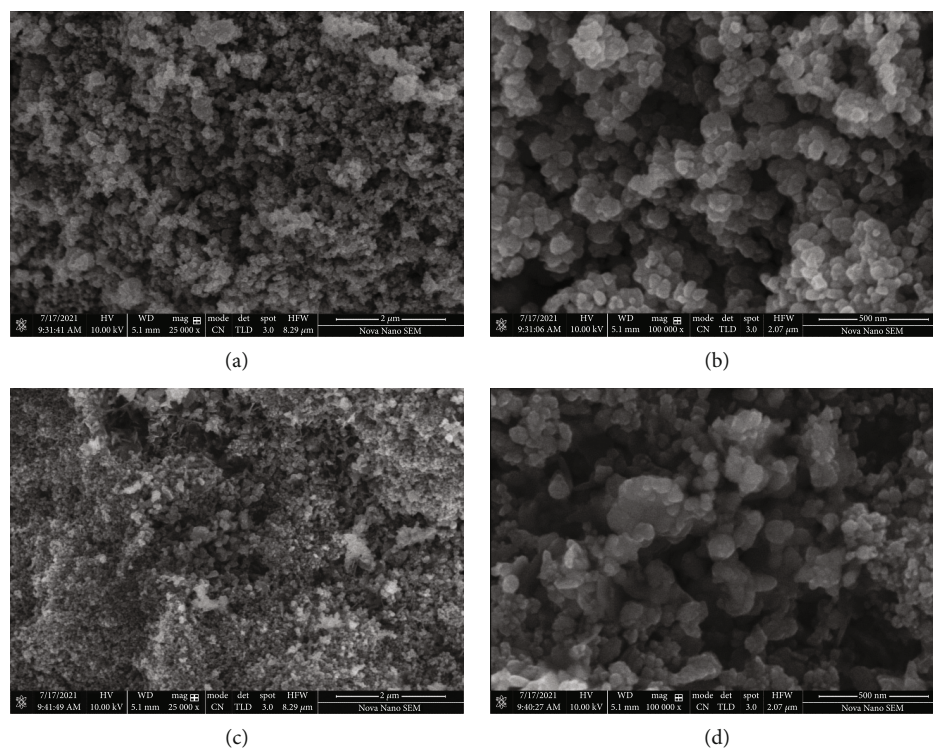
FIGURE 4: FESEM topographical analysis (surface view) of (a, b) pure ZnO and (c, d) Mn-doped ZnO at 25kx and 100kx magnification scales, respectively.
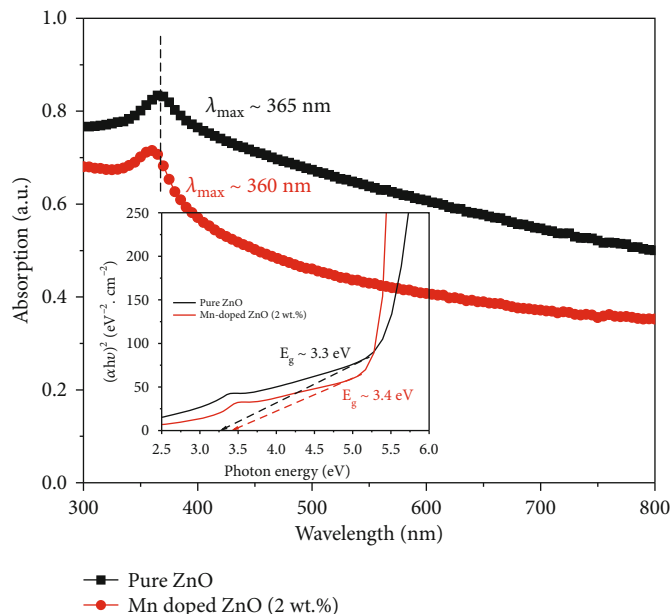

FIGURE 5: The UV-vis absorption spectra of pure and Mn-doped ZnO nanoparticles and (inset) the bandgap estimation of synthesized samples via Tauc plot.

near UV wavelength range, we have investigated the capability of both photocatalysts in the presence of solar light irradiation instead of visible light, alone.

The Brunauer–Emmett–Teller (BET) method is ubiquitously utilized in nanotechnology and is envisaged to be an ideal experimental tool to estimate the specific surface area of the nanomaterials [65]. In the present study, a linear BET multipoint plot of $1/[W(P/P_o) - 1]$ vs. P/P_o has been obtained for both pure and Mn-doped ZnO photocatalysts. In multipoint BET analysis, five or a minimum of three data

ZnO photocatalyst
sample weight (w) ~ 0.6611 g

Equation	$y = a + b*x$		
Weight	No weighting		
Residual sum of squares	0.05899		
Adj. R-square	0.99997		
		Value	Standard error
E	Intercept	1.74476	0.08759
E	Slope	201.82549	0.47856

(a)

Mn-doped ZnO photocatalyst
sample weight (w) ~ 0.3445 g

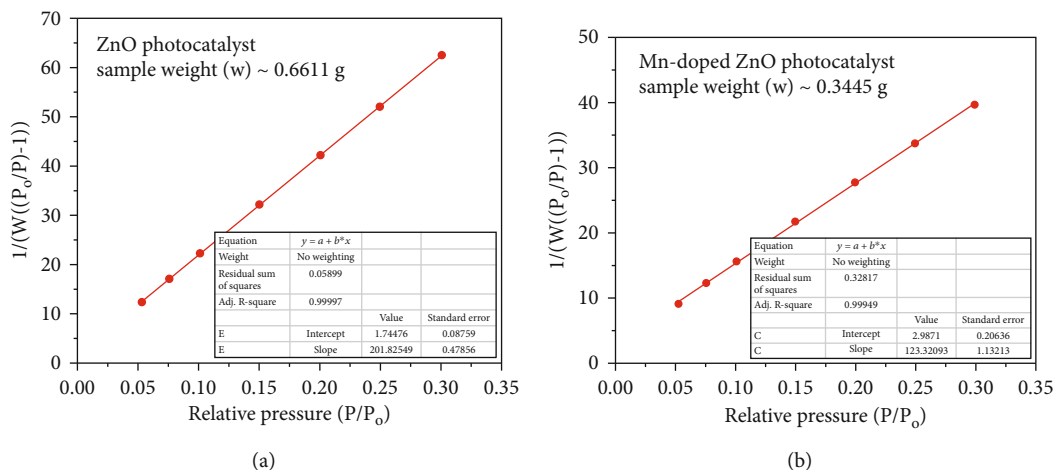| Equation	$y = a + b*x$		
Weight	No weighting		
Residual sum of squares	0.32817		
Adj. R-square	0.99949		
		Value	Standard error
C	Intercept	2.9871	0.20636
C	Slope	123.32093	1.13213

(b)

FIGURE 6: Linear plot of BET equation to determine the surface area of (a) pure ZnO and (b) Mn-doped ZnO nanoparticles.

points are typically used in the P/P_o range~0.025 to 0.30, to successfully determine the surface area [66], using the BET equation expressed as [67]

$$\frac{1}{[W(P/P_o) - 1]} = \frac{1}{W_m C} + \frac{C - 1}{W_m C}(P/P_o), \qquad (3)$$

where "W" is the weight of adsorbed gas, "P/P_o" is the relative pressure, "C" is the BET constant, and "W_m" is the weight of the absorbate as a monolayer. Furthermore, the linear plot of the multipoint BET equation may be used to calculate the slope (s) and intercept (i) as expressed in Figure 6. The mathematical expressions for s, i, and W_m are as follows:

$$s = \frac{C - 1}{W_m C}, \qquad (4)$$

$$i = \frac{1}{W_m C}, \qquad (5)$$

$$W_m = \frac{1}{s + i}. \qquad (6)$$

The specific surface area of both synthesized photocatalysts may thus be mathematically determined by the following equation:

$$S_{BET} = \frac{W_m N_a A_{cs}}{wM}, \qquad (7)$$

whereby "N_a" represents Avogadro's number (i.e., 6.022×10^{23}), "A_{cs}" is the adsorbate nitrogen cross-sectional area (i.e., 16.200 Å^2), "M" is the molecular weight of the absorbate nitrogen gas (i.e., 28.013 g/mol), and "w" is the utilized sample weight. Through Equation (7), the specific surface area (S_{BET}) of pure and Mn-doped ZnO has been calculated to be 25.804 m^2/g and 79.834 m^2/g. The significant increase in the S_{BET} of the Mn-doped ZnO photocatalyst may be understood in terms of the crystallite size. A similar increasing

trend of specific surface area has been previously reported with decreasing crystallite size in various studies [68, 69]. Zhang et al. previously observed a similar consistent correlation between crystallite size and specific surface area for TiO$_2$ nanoparticles subjected to various heat-treatment temperatures [70]. It is pertinent to mention that in general, the smaller nanoparticles exhibit superior photocatalytic performance owing to their higher specific surface area [71]. With the decrease in the size of nanoparticles, the reactivity and the percentage of atoms on the surface of nanoparticles increase, and hence, an increase in the photocatalytic activity is observed.

Figure 7 depicts the UV-vis absorption spectrum of MG dye (solution state in DI water) which implies the strong distinctive absorption peak positioned at λ_{max}~620 nm, accompanied by two prominent shoulder peaks at 315 and 425 nm, respectively [16, 72, 73]. The shoulder peaks correspond to benzoic rings in the dye structure [74]. Specifically, the weaker absorption peak in the near UV region (i.e., at 315 nm) may be ascribed to n-π * transitions [75]. The photocatalytic activity of MG dye solution has been studied, mediated by the pure and Mn-doped ZnO, at the reference wavelength of 620 nm which corresponds to the absorption maximum of MG dye.

During the PCA study, primarily, the light absorption characteristics of the pure MG aqueous solution (devoid of any photocatalyst) have been examined, under natural sunlight irradiation (illumination time = 60 minutes). In general, quite an insignificant decline in the absorption maximum of MG dye solution has been observed, which affirms that there is a diminutive decrease in MG dye concentration due to the photolysis phenomenon [16, 76]. Later, the absorption peak of MG aqueous solution has also been monitored in the presence of both catalysts (pure and Mn-doped ZnO nanoparticles) under natural sunlight illumination (60 minutes duration). During this activity, ~3 mL of the reaction sample aliquots has been sequentially drawn (each, after a regular 10 mins time interval) and subjected to spectrophotometric study by UV-vis absorption spectroscopy. Figure 8(a) depicts the relative concentration (C_t/C_o)
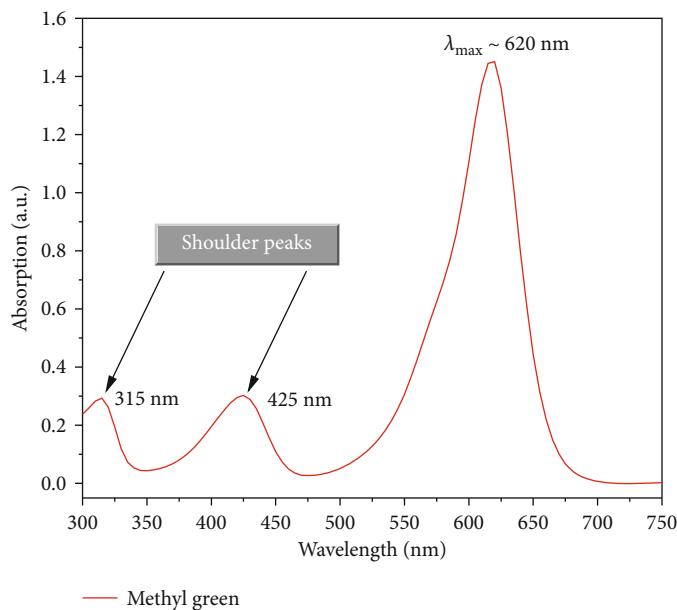
FIGURE 7: The solution state (DI water) absorption spectrum of methyl green pollutant dye.

of MG dye solution in response to the irradiation time, in the presence of pure and Mn-doped ZnO nanoparticles. Here, "C_o" symbolizes the original concentration of MG dye solution before sunlight irradiation, and "C_t" signifies the residual concentration of the solution after irradiation for time (t). In general, it has been observed that under the influence of natural sunlight irradiation, the MG solution progressively loses its characteristic green color in the presence of photocatalysts. The progressive decrease in the reaction sample's absorption maximum (at $\lambda_{max} = 620$ nm) with increased irradiation time may be ascribed to the photodegradation of the MG dye [73, 77]. It is well understood that, as reaction time proceeds, the mutual interaction between the MG dye molecule and the surface of photocatalysts also increases, which effectively enhances the photodegradation of the pollutant dye [78].

It may be easily observed from Figure 8(a) that both photocatalysts exhibit significant photocatalytic properties toward the degradation of MG pollutant dye. However, the photocatalytic performance of ZnO has been observed to improve substantially with Mn-doping. For detailed analysis, the photocatalytic degradation kinetics of MG dye has been investigated in time "t," to estimate the photocatalytic reaction rate constant (K) and correlation coefficient (R^2). The experimental data have been analyzed by the kinetic models, such as pseudo-first-order and pseudo-second-order.

The linear expression for the pseudo-first-order is mathematically expressed as [79]

$$\ln (C_o/C_t) = K_1 t. \tag{8}$$

The value of "K_1" has been calculated (from Figure 8(b)) by estimating the slope of the plot between irradiation time and $\ln (C_o/C_t)$. Specifically, the rate of photocatalytic reaction (K_1) ~0.01477 min^{-1} and R^2~0.92164 has been achieved for

pure ZnO, whereas slightly higher ~0.01617 min^{-1} and R^2 ~0.93494 have been observed for Mn-doped ZnO, respectively. Here, it may be observed that the value of R^2 (in both cases) is significantly lower than that of unity and hence unacceptable.

Contrariwise, the pseudo-second-order relation may be expressed as

$$((1/C_t) - (1/C_o)) = K_2 t. \tag{9}$$

The slope of graphs (presented in Figure 8(c)) helps to find out the values of the second-order rate constant (K_2) for pure and Mn-doped ZnO photocatalysts. The data represented in the graph (Figure 8(c)) clearly shows that the K_2 value in the case of pure ZnO is 0.01792 min^{-1}, and for Mn-doped ZnO, it is comparatively higher, i.e., 0.02072 min^{-1}. Furthermore, the R^2 values for the pseudo-second-order reaction kinetic model are 0.97992 and 0.97299 for pure and Mn-doped ZnO photocatalysts, respectively, which are relatively adequate.

Figure 8(d) compares the photocatalytic performance of both catalysts. It may be observed that after 60 min irradiation of natural sunlight, ~62.78% and ~66.44% photocatalytic degradation of MG aqueous solution has been achieved mediated by pure and Mn-doped (2 wt. %) ZnO photocatalyst, respectively. It may be established from Figure 8 that Mn-doped ZnO nanoparticles exhibit distinctly higher PCA efficiency of MG dye as compared to pure ZnO. Earlier, Li. et al. have also obtained similar results in a study that investigates the potential of pure and Mn-doped ZnO photocatalysts towards methyl orange dye (MO) degradation. In their study, the superior photocatalytic activity of Mn-doped ZnO has been ascribed to the dopant ions, which not only provide impurity energy levels but also serve as electron trapping sites to promote the separation and restrain the recombination of photogenerated charge carriers [80].
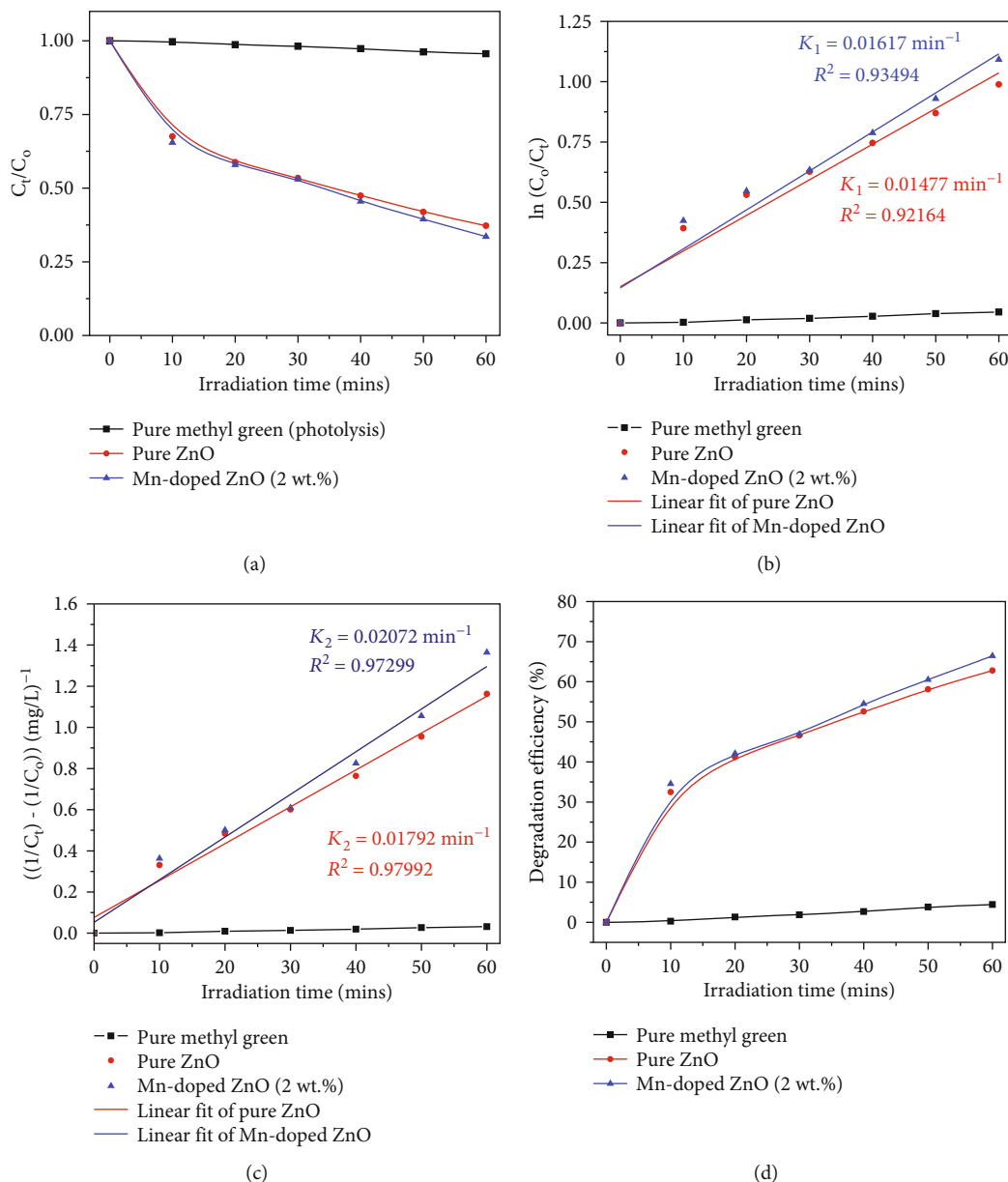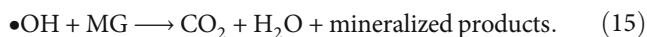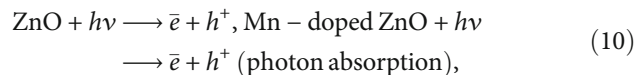
(a)

(b)

(c)

(d)

FIGURE 8: The photodegradation of MG dye mediated by pure and Mn-doped ZnO nanoparticles (a) normalized C_t/C_o curves, (b) plot of $\ln(C_o/C_t)$, (c) second-order reaction kinetics, and (d) dye degradation (%) as a function of irradiation time, respectively.

It is one of the major drawbacks of ZnO photocatalyst that the rate of electron-hole recombination is significantly higher [81]. Doping ZnO lattice with transition metals typically introduces intermediate energy states, wherein electrons might get trapped, thereby impeding the probabilities of electron-hole pair recombination [82]. For instance, Ibanescu et al. have previously confirmed a relatively blue shift in absorption with the manganese doping in ZnO and a reduction in the possibility of electron-hole pair recombination [83]. Similarly, Gupta et al. have also confirmed that the synergistic interactions with multiple charge transfer pathways may considerably enhance the PCA efficiency of the Mn-doped ZnO photocatalyst [84].

The photodegradation mechanism of methyl green dye mediated by synthesized photocatalysts (pure and Mn-doped ZnO) under sunlight may be described by the following successive reactions:

$$ZnO + h\nu \longrightarrow \bar{e} + h^+, \text{Mn} - \text{doped ZnO} + h\nu \\ \longrightarrow \bar{e} + h^+ \text{ (photon absorption)}, \tag{10}$$

$$\bar{e} + h^+ \longrightarrow \text{Heat (undesired recombination)}, \tag{11}$$

$$\bar{e} + O_2 \longrightarrow O_2^{-\bullet} \text{ (superoxide anion formation)}, \tag{12}$$

$$h^+ + OH^- \longrightarrow \bullet OH \text{ (Hydroxyl radical formation)}, \tag{13}$$

$$O_2^{-\bullet} + H_2O \longrightarrow \bullet OH, \tag{14}$$

$$\bullet OH + MG \longrightarrow CO_2 + H_2O + \text{mineralized products}. \tag{15}$$
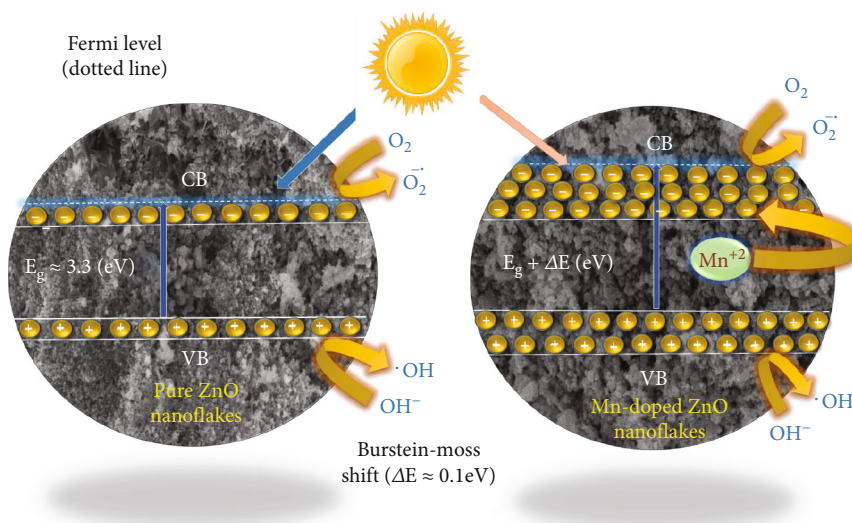
Figure 9: Schematic representation of the Burstein-Moss effect in Mn-doped ZnO nanoparticles.

Table 2: Comparison of photocatalytic performance of synthesized photocatalysts with literature.

Light source (time)	Pollutant dye (concentration)	Photocatalyst	Catalyst amount	Rate constant (K)	Degradation efficiency	Ref.
UV (60 min)	Malachite green (15 ppm)	Ni-doped ZnO (6 wt. %)	0.1 g/L	0.0042 min^{-1}	76%	[92]
UV (120 min)	Methyl green (40 ppm)	Nickel-dimethylglyoxime/ZSM-5 zeolite	0.6 g/L	0.036 min^{-1}	76.5%	[93]
Visible (50 min)	Methyl green	Cu-doped ZnO (5 wt. %)	—	0.04 min^{-1}	75%	[94]
UV (50 min)	Methyl green	Tb-doped ZnO (1 wt. %)	—	0.022 min^{-1}	77%	[95]
UV (120 min)	Methylene blue (10 ppm)	Mn-doped ZnO (2 wt. %)	0.3 g/L	0.03 min^{-1}	99%	[82]
Natural sunlight (240 min)	Congo red (100 ppm)	Mn-doped ZnO (7 wt. %)	1 g/L	0.0089 min^{-1}	87%	[24]
Natural sunlight (60 min)	Methyl green (20 ppm)	Pure ZnO	0.1 g/L	0.01792 min^{-1}	62.78%	Present study
Natural sunlight (60 min)	Methyl green (20 ppm)	Mn-doped ZnO (2 wt. %)	0.1 g/L	0.02072 min^{-1}	66.44%	Present study

In the first step, when a photon having energy equaling or exceeding the bandgap energy (E_g) of photocatalysts (pure and Mn-doped ZnO) is absorbed, an electron (e^-) is excited from the valence band (VB) and gets transferred to the empty conduction band (CB), creating a hole vacancy (h^+) in the VB (as in Equation (10)). In the second step, these photoinduced charge carriers may migrate to the active sites of the surface of the photocatalyst, where they act as reducing/oxidizing agents to facilitate redox reactions on the surface. Specifically, the electrons react with oxygen to produce superoxide anion, whereas the holes react with water and hydroxide ions to produce hydroxyl radicals (as expressed in Equations (13) and (14), respectively) [85]. However, numerous studies have previously indicated that pure ZnO (as a photocatalyst) exhibits low-charge separation efficiency [85, 86]. Hence, photoinduced e^-/h^+ pairs in ZnO may inevitably recombine producing heat as wasted energy. Moreover, since the recombination process is much faster than the charge transportation to the active sites, this ultimately results in reduced photocatalytic efficiency of ZnO [87]. The recombination process inhibits the photocatalytic performance of ZnO, since only a limited number of photoinduced charge carriers produce the active radicals (•OH and $O_2^{-•}$) which are essentially required for the degradation of the MG dye pollutants [73]. It is also pertinent to mention that hydroxyl radicals are strong oxidizing agents and may oxidize nearly all organic pollutant dyes with no selectivity [88].

Contrariwise, when ZnO is doped with manganese atoms, the dopant ions replace Zn ions in the host lattice and tend to act like electron scavengers. The difference in the bandgap of pure and Mn-doped ZnO is a direct indication of the variation in the electronic structure of hexagonal ZnO with Mn^{2+} substitution [89]. The widening of the bandgap may be attributed to the Burstein-Moss effect, which causes a shifting in the position of the Fermi level into the conduction band (as shown in Figure 9). Specifically, the shift of Fermi level is the consequence of the Pauli exclusion principle, since the enhanced charge carrier concentration (sourced by Mn-doping) results in the occupancy of the

low energy levels closer to the conduction band [64]. Resultantly, the low energy transitions are blocked, since the Pauli exclusion principle forbids excitation into the preoccupied states, and resultantly, the apparent bandgap is increased (where apparent bandgap = bandgap energy (Eg) + Burstein − Moss shift (ΔE)). Furthermore, it is well understood that the metal dopant atoms (in particular the transition metals like Mn) change the coordination environment of ZnO and create surface defects in the ZnO host [25]. The defect states subsequently trap excited electrons and improve the separation of photogenerated e^-/h^+ pair [90, 91]. The improved photocatalytic activity of Mn-doped ZnO may therefore easily be attributed to the prominent e^-/h^+ pair separation ability and subsequent efficient generation of hydroxyl radicals vital for effective dye degradation.

Table 2 compares the photocatalytic activity of the synthesized photocatalysts (pure and Mn-doped ZnO) with the literature.

4. Conclusion

In this study, we have utilized the chemical precipitation method to synthesize pure and Mn-doped ZnO (2 wt. %) nanoparticles for photodegradation (of methyl green pollutant dye). The XRD structural analysis has revealed the hexagonal wurtzite structure of both as-synthesized intrinsic and extrinsic (Mn-doped) ZnO photocatalysts. The investigation of photophysical properties by UV-vis indicates that the absorption peak in Mn-doped ZnO nanoparticles is blue-shifted by 5 nm ($365 \rightarrow 360$ nm), due to the widening of the bandgap, which has been attributed to the Burstein-Moss effect instead of quantum confinement. Furthermore, the BET analysis has revealed that the specific surface area (S_{BET}) Mn-doped ZnO (79.834 m^2/g) is three-fold higher as compared to that of pure ZnO (25.804 m^2/g), which is considered to be an advantage as it provides a relatively more active area for photocatalytic reaction. In photocatalytic activity calculations, following the pseudo-second-order reaction kinetic model, the rates of photocatalytic reactions (K_2) have been observed to be 0.01792 min^{-1} and 0.02072 min^{-1} for pure and Mn-doped Zn, respectively. After 60 minutes of natural sunlight irradiation, pure and Mn-doped (2 wt. %) ZnO photocatalysts were found to achieve 62.78 percent and 66.44 percent photocatalytic degradation of MG aqueous solution, respectively. The current findings show that doping pure ZnO nanoparticles with manganese improves their photocatalytic properties by 5.83 percent over intrinsic ZnO. In summary, the synergistic interactions with multiple charge transfer pathways, improvement of e^-/h^+ pair charge separation, enhanced surface area, and efficient generation of hydroxyl radicals are supposed to be responsible for the considerably higher photocatalytic efficiency of the Mn-doped ZnO photocatalyst.

Data Availability

All data has already been provided in the form of ORIGIN plots. Further requested data can be made available upon the reader's request.

Ethical Approval

Neither there are potential risks and ethical issues involved in the current research, nor the authors have engaged in any form of malicious harm to another person or animal.

Conflicts of Interest

The authors declare no conflict of interest.

Acknowledgments

References

[1] S. Taghavi Fardood, F. Moradnia, R. Forootan et al., "Facile green synthesis, characterization and visible light photocatalytic activity of MgFe$_2$O$_4$@CoCr$_2$O$_4$ magnetic nanocomposite," *Journal of Photochemistry and Photobiology A: Chemistry*, vol. 423, article 113621, 2022.

[2] A. H. Alibak, M. Khodarahmi, P. Fayyazsanavi, S. M. Alizadeh, A. J. Hadi, and E. Aminzadehsarikhanbeglou, "Simulation the adsorption capacity of polyvinyl alcohol/carboxymethyl cellulose based hydrogels towards methylene blue in aqueous solutions using cascade correlation neural network (CCNN) technique," *Journal of Cleaner Production*, vol. 337, article 130509, 2022.

[3] A. Rafiq, M. Ikram, S. Ali et al., "Photocatalytic degradation of dyes using semiconductor photocatalysts to clean industrial water pollution," *Journal of Industrial and Engineering Chemistry*, vol. 97, pp. 111–128, 2021.

[4] F. Moradnia, S. Taghavi Fardood, A. Ramazani, B. K. Min, S. W. Joo, and R. S. Varma, "Magnetic Mg0.5Zn0.5FeMnO4 nanoparticles: green sol-gel synthesis, characterization, and photocatalytic applications," *Journal of Cleaner Production*, vol. 288, article 125632, 2021.

[5] M. Adeel, M. Saeed, I. Khan, M. Muneer, and N. Akram, "Synthesis and characterization of co–ZnO and evaluation of its photocatalytic activity for photodegradation of methyl orange," *ACS Omega*, vol. 6, no. 2, pp. 1426–1435, 2021.

[6] N. M. Mahmoodi, "Synthesis of magnetic carbon nanotube and photocatalytic dye degradation ability," *Environmental Monitoring and Assessment*, vol. 186, no. 9, pp. 5595–5604, 2014.

[7] A. Gupta, S. A. Khan, and T. A. Khan, "Remediation of textile wastewater by ozonation," in *Sustainable Practices in the Textile Industry*, L. Jameel Rather, M. Shabbir, and A. Haji, Eds., pp. 273–284, Scrivener-Wiley, USA, 2021.

[8] R. S. Dassanayake, S. Acharya, and N. Abidi, "Recent advances in biopolymer-based dye removal technologies," *Molecules*, vol. 26, no. 15, p. 4697, 2021.

[9] B. Qiu, Y. Hu, C. Tang, Y. Chen, and J. Cheng, "Degradation of diclofenac via sequential reduction-oxidation by Ru/Fe modified biocathode dual-chamber bioelectrochemical system: performance, pathways and degradation mechanisms," *Chemosphere*, vol. 291, Part 2, article 132881, 2022.

[10] P. Compton, N. R. Dehkordi, M. Knapp, L. A. Fernandez, A. N. Alshawabkeh, and P. Larese-Casanova, "Heterogeneous

Fenton-like catalysis of electrogenerated H2O2 for dissolved RDX removal," *Frontiers in Chemical Engineering*, vol. 4, 2022.

[11] M. J. Uddin, R. E. Ampiaw, and W. Lee, "Adsorptive removal of dyes from wastewater using a metal-organic framework: a review," *Chemosphere*, vol. 284, article 131314, 2021.

[12] J. Ou, J. Yan, T. Xu et al., "Fabrication of nickel-iron layered double hydroxides using nickel plating wastewater via electro-coagulation, and its use for efficient dye removal," *Journal of Molecular Liquids*, vol. 335, article 116246, 2021.

[13] S. Asha, T. C. Bessy, J. F. Joe Sherin et al., "Efficient photocatalytic degradation of industrial contaminants by _Piper longum_ mediated ZnO nanoparticles," *Environmental Research*, vol. 208, article 112686, 2022.

[14] K. Sun, L. Wang, C. Wu, J. Deng, and K. Pan, "Fabrication of α-Fe$_2$O$_3$@rGO/PAN nanofiber composite membrane for photocatalytic degradation of organic dyes," *Advanced Materials Interfaces*, vol. 4, no. 24, article 1700845, 2017.

[15] S. Dolatabadi, M. Fattahi, and M. Nabati, "Solid state dispersion and hydrothermal synthesis, characterization and evaluations of TiO2/ZnO nanostructures for degradation of rhodamine B," *Desalination and Water Treatment*, vol. 231, pp. 425–435, 2021.

[16] H. Bel Hadjltaief, M. Ben Zina, M. E. Galvez, and P. da Costa, "Photocatalytic degradation of methyl green dye in aqueous solution over natural clay-supported ZnO-TiO$_2$ catalysts," *Journal of Photochemistry and Photobiology A: Chemistry*, vol. 315, pp. 25–33, 2016.

[17] J. Yu and X. Yu, "Hydrothermal synthesis and photocatalytic activity of zinc oxide hollow spheres," *Environmental Science & Technology*, vol. 42, no. 13, pp. 4902–4907, 2008.

[18] W. Shen, Z. Li, H. Wang, Y. Liu, Q. Guo, and Y. Zhang, "Photocatalytic degradation for methylene blue using zinc oxide prepared by codeposition and sol-gel methods," *Journal of Hazardous Materials*, vol. 152, no. 1, pp. 172–175, 2008.

[19] H. Asadzadeh Patehkhor, M. Fattahi, and M. Khosravi-Nikou, "Synthesis and characterization of ternary chitosan- TiO$_2$-ZnO over graphene for photocatalytic degradation of tetracycline from pharmaceutical wastewater," *Scientific Reports*, vol. 11, no. 1, p. 24177, 2021.

[20] C. Sushma and S. Girish Kumar, "Advancements in the zinc oxide nanomaterials for efficient photocatalysis," *Chemical Papers*, vol. 71, no. 10, pp. 2023–2042, 2017.

[21] A. Das, S. K. Nikhil, and R. G. Nair, "Influence of surface morphology on photocatalytic performance of zinc oxide: a review," *Nano-Structures & Nano-Objects*, vol. 19, article 100353, 2019.

[22] K. Dai, G. Dawson, S. Yang, Z. Chen, and L. Lu, "Large scale preparing carbon nanotube/zinc oxide hybrid and its application for highly reusable photocatalyst," *Chemical Engineering Journal*, vol. 191, pp. 571–578, 2012.

[23] J. Z. Bloh, R. Dillert, and D. W. Bahnemann, "Zinc oxide photocatalysis: influence of iron and titanium doping and origin of the optimal doping ratio," *ChemCatChem*, vol. 5, no. 3, pp. 774–778, 2013.

[24] P. S. Vindhya, R. Kunjikannan, and V. T. Kavitha, "Photocatalytic and antimicrobial activities of pure and Mn doped ZnO nanoparticles synthesised by *Annona muricata* leaf extract," *International Journal of Environmental Analytical Chemistry*, pp. 1–16, 2022.

[25] K. Rekha, M. Nirmala, M. G. Nair, and A. Anukaliani, "Structural, optical, photocatalytic and antibacterial activity of zinc oxide and manganese doped zinc oxide nanoparticles," *Physica B: Condensed Matter*, vol. 405, no. 15, pp. 3180–3185, 2010.

[26] R. Ullah and J. Dutta, "Photocatalytic degradation of organic dyes with manganese-doped ZnO nanoparticles," *Journal of Hazardous Materials*, vol. 156, no. 1-3, pp. 194–200, 2008.

[27] R. Akram, Z. M. Almohaimeed, A. Bashir, M. Ikram, K. W. Qadir, and Q. Zafar, "Synthesis and characterization of pristine and strontium-doped zinc oxide nanoparticles for methyl green photo-degradation application," *Nanotechnology*, vol. 33, no. 29, article 295702, 2022.

[28] A. Mirzaei, L. Yerushalmi, Z. Chen, F. Haghighat, and J. Guo, "Enhanced photocatalytic degradation of sulfamethoxazole by zinc oxide photocatalyst in the presence of fluoride ions: optimization of parameters and toxicological evaluation," *Water Research*, vol. 132, pp. 241–251, 2018.

[29] B. R. Cruz-Ortiz, J. W. J. Hamilton, C. Pablos et al., "Mechanism of photocatalytic disinfection using titania-graphene composites under UV and visible irradiation," *Chemical Engineering Journal*, vol. 316, pp. 179–186, 2017.

[30] M. Musharaf, S. Karamat, M. U. Hassan et al., "Solubility enhancement of Fe in ZnO nanoparticles prepared by co-precipitation method," *Journal of Superconductivity and Novel Magnetism*, vol. 34, no. 10, pp. 2633–2642, 2021.

[31] M. Ikram, S. Aslam, A. Haider et al., "Doping of Mg on ZnO nanorods demonstrated improved photocatalytic degradation and antimicrobial potential with molecular docking analysis," *Nanoscale Research Letters*, vol. 16, no. 1, pp. 1–16, 2021.

[32] T. P. Yoon, M. A. Ischay, and J. Du, "Visible light photocatalysis as a greener approach to photochemical synthesis," *Nature Chemistry*, vol. 2, no. 7, pp. 527–532, 2010.

[33] W. Subramonian and T. Y. Wu, "Effect of enhancers and inhibitors on photocatalytic sunlight treatment of methylene blue," *Water, Air, & Soil Pollution*, vol. 225, no. 4, p. 1922, 2014.

[34] R. Beura, R. Pachaiappan, and P. Thangadurai, "A detailed study on Sn^{4+} doped ZnO for enhanced photocatalytic degradation," *Applied Surface Science*, vol. 433, pp. 887–898, 2018.

[35] K. Munawar, M. A. Mansoor, M. M. Olmstead et al., "Fabrication of Ag-ZnO composite thin films for plasmonic enhanced water splitting," *Materials Chemistry and Physics*, vol. 255, article 123220, 2020.

[36] S. Talam, S. R. Karumuri, and N. Gunnam, "Synthesis, characterization, and spectroscopic properties of ZnO nanoparticles," *ISRN Nanotechnology*, vol. 2012, Article ID 372505, 6 pages, 2012.

[37] D. Ghica, I. D. Vlaicu, M. Stefan, V. A. Maraloiu, A. C. Joita, and C. Ghica, "Tailoring the dopant distribution in ZnO:Mn nanocrystals," *Scientific Reports*, vol. 9, no. 1, p. 6894, 2019.

[38] S. D. Birajdar, R. C. Alange, S. D. More, V. D. Murumkar, and K. M. Jadhav, "Sol-gel auto combustion synthesis, structural and magnetic properties of Mn doped ZnO nanoparticles," *Procedia Manufacturing*, vol. 20, pp. 174–180, 2018.

[39] K. Omri, J. el Ghoul, O. M. Lemine, M. Bououdina, B. Zhang, and L. el Mir, "Magnetic and optical properties of manganese doped ZnO nanoparticles synthesized by sol-gel technique," *Superlattices and Microstructures*, vol. 60, pp. 139–147, 2013.

[40] G. Vijayaprasath, R. Murugan, S. Asaithambi et al., "Structural and magnetic behavior of Ni/Mn co-doped ZnO nanoparticles prepared by co-precipitation method," *Ceramics International*, vol. 42, no. 2, pp. 2836–2845, 2016.

[41] O. Bilgili, "The effects of Mn doping on the structural and optical properties of ZnO," *Acta Physica Polonica, A.*, vol. 136, no. 3, pp. 460–466, 2019.

[42] J. Panda, I. Sasmal, and T. K. Nath, "Magnetic and optical properties of Mn-doped ZnO vertically aligned nanorods synthesized by hydrothermal technique," *AIP Advances*, vol. 6, no. 3, article 035118, 2016.

[43] R. Sivasankari, M. Elango, J. Varuna, and K. Thamizharasan, "Evaluation of physical properties and bactericidal efficacy of chemically developed undoped and Mn (5, 10, 15wt%) doped ZnO nanoparticles," *Materials Technology*, vol. 37, no. 5, pp. 316–323, 2022.

[44] P. Kumar, B. K. Singh, B. N. Pal, and P. C. Pandey, "Correlation between structural, optical and magnetic properties of Mn-doped ZnO," *Applied Physics A*, vol. 122, no. 8, p. 740, 2016.

[45] S. K. Kansal and P. Prerna, "Preparation, characterization and photocatalytic activity of ZnO and Mn doped ZnO nanoparticles," *Focus*, vol. 2, no. 3, pp. 203–207, 2013.

[46] A. Srithar, J. Kannan, and T. Senthil, "Synthesis, structural and optical properties of Mn doped ZnO nanoparticles and their antibacterial application," *Journal of Advances in Chemistry*, vol. 12, no. 12, 2016.

[47] M. Shatnawi, A. M. Alsmadi, I. Bsoul et al., "Influence of Mn doping on the magnetic and optical properties of ZnO nanocrystalline particles," *Results in Physics*, vol. 6, pp. 1064–1071, 2016.

[48] A. A. Othman, M. A. Osman, E. M. M. Ibrahim, M. A. Ali, and A. G. Abd-Elrahim, "Mn-doped ZnO nanocrystals synthesized by sonochemical method: structural, photoluminescence, and magnetic properties," *Materials Science and Engineering: B*, vol. 219, pp. 1–9, 2017.

[49] V. Mote, J. Dargad, and B. Dole, "Effect of Mn doping concentration on structural, morphological and optical studies of ZnO nano-particles," *Nanoscience and Nanoengineering*, vol. 1, no. 2, pp. 116–122, 2013.

[50] R. Das and S. Sarkar, "Determination of intrinsic strain in poly (vinylpyrrolidone)-capped silver nano-hexapod using X-ray diffraction technique," *Current Science*, vol. 109, no. 4, pp. 775–778, 2015.

[51] P. Shunmuga Sundaram, T. Sangeetha, S. Rajakarthihan, R. Vijayalaksmi, A. Elangovan, and G. Arivazhagan, "XRD structural studies on cobalt doped zinc oxide nanoparticles synthesized by coprecipitation method: Williamson-Hall and size-strain plot approaches," *Physica B: Condensed Matter*, vol. 595, article 412342, 2020.

[52] S. Mustapha et al., "Comparative study of crystallite size using Williamson-Hall and Debye-Scherrer plots for ZnO nanoparticles," *Advances in Natural Sciences: Nanoscience and Nanotechnology*, vol. 10, no. 4, article 045013, 2019.

[53] D. Nath, F. Singh, and R. Das, "X-ray diffraction analysis by Williamson-Hall, Halder-Wagner and size-strain plot methods of CdSe nanoparticles- a comparative study," *Materials Chemistry and Physics*, vol. 239, article 122021, 2020.

[54] H. Irfan, K. Mohamed Racik, and S. Anand, "Microstructural evaluation of CoAl$_2$O$_4$ nanoparticles by Williamson–Hall and size–strain plot methods," *Journal of Asian Ceramic Societies*, vol. 6, no. 1, pp. 54–62, 2018.

[55] P. Nwaokafor, K. B. Okeoma, O. K. Echendu, A. C. Ohajianya, and K. O. Egbo, "X-ray Diffraction Analysis of a Class of AlMgCu Alloy Using Williamson–Hall and Scherrer Methods," *Metallography, Microstructure, and Analysis*, vol. 10, 2021.

[56] E. Emil and S. Gürmen, "Estimation of yttrium oxide microstructural parameters using the Williamson–Hall analysis," *Materials Science and Technology*, vol. 34, no. 13, pp. 1549–1557, 2018.

[57] B. Manikandan, T. Endo, S. Kaneko, K. R. Murali, and R. John, "Properties of sol gel synthesized ZnO nanoparticles," *Journal of Materials Science: Materials in Electronics*, vol. 29, no. 11, pp. 9474–9485, 2018.

[58] A. Sinhamahapatra, A. K. Giri, P. Pal, S. K. Pahari, H. C. Bajaj, and A. B. Panda, "A rapid and green synthetic approach for hierarchically assembled porous ZnO nanoflakes with enhanced catalytic activity," *Journal of Materials Chemistry*, vol. 22, no. 33, pp. 17227–17235, 2012.

[59] B. Wu, J. Li, and Q. Li, "Preparation and photoluminescence behavior of Mn-doped nano-ZnO," *Optik*, vol. 188, pp. 205–211, 2019.

[60] S. Husain, L. A. Alkhtaby, E. Giorgetti, A. Zoppi, and M. Muniz Miranda, "Effect of Mn doping on structural and optical properties of sol gel derived ZnO nanoparticles," *Journal of Luminescence*, vol. 145, pp. 132–137, 2014.

[61] R. Viswanatha, S. Sapra, S. Sen Gupta et al., "Synthesis and characterization of Mn-doped ZnO nanocrystals," *The Journal of Physical Chemistry B*, vol. 108, no. 20, pp. 6303–6310, 2004.

[62] N. Wang, Y. Yang, and G. Yang, "Great blue-shift of luminescence of ZnO nanoparticle array constructed from ZnO quantum dots," *Nanoscale Research Letters*, vol. 6, no. 1, pp. 338–338, 2011.

[63] V. H.-T. Thi and B.-K. Lee, "Effective photocatalytic degradation of paracetamol using La-doped ZnO photocatalyst under visible light irradiation," *Materials Research Bulletin*, vol. 96, pp. 171–182, 2017.

[64] R. Ponnusamy, S. C. Selvaraj, M. Ramachandran, P. Murugan, P. M. G. Nambissan, and D. Sivasubramanian, "Diverse spectroscopic studies and first-principles investigations of the zinc vacancy mediated ferromagnetism in Mn-doped ZnO nanoparticles," *Crystal Growth & Design*, vol. 16, no. 7, pp. 3656–3668, 2016.

[65] S. A. Aldahash, P. Higgins, S. Siddiqui, and M. K. Uddin, "Fabrication of polyamide-12/cement nanocomposite and its testing for different dyes removal from aqueous solution: characterization, adsorption, and regeneration studies," *Scientific Reports*, vol. 12, no. 1, p. 13144, 2022.

[66] N. Hwang and A. R. Barron, "BET surface area analysis of nanoparticles," in *The Connexions Project (open repository of educational materials)*, pp. 1–11, Rice University: Houston, TX, USA, 2021.

[67] C. T. Chiou, J. F. Lee, and S. A. Boyd, "The surface area of soil organic matter," *Environmental Science & Technology*, vol. 24, no. 8, pp. 1164–1166, 1990.

[68] K. Okada, T. Nagashima, Y. Kameshima, A. Yasumori, and T. Tsukada, "Relationship between formation conditions, properties, and crystallite size of boehmite," *Journal of Colloid and Interface Science*, vol. 253, no. 2, pp. 308–314, 2002.

[69] D. Banham, S. Ye, T. Cheng et al., "Effect of CeOx crystallite size on the chemical stability of CeOx nanoparticles," *Journal of the Electrochemical Society*, vol. 161, no. 10, pp. F1075–F1080, 2014.

[70] Z. Zhang, S. Brown, J. B. M. Goodall et al., "Direct continuous hydrothermal synthesis of high surface area nanosized titania,"

Journal of Alloys and Compounds, vol. 476, no. 1-2, pp. 451–456, 2009.

[71] Y. Liu, Q. Zhang, M. Xu et al., "Novel and efficient synthesis of Ag-ZnO nanoparticles for the sunlight-induced photocatalytic degradation," *Applied Surface Science*, vol. 476, pp. 632–640, 2019.

[72] V. Chandraboss, B. Karthikeyan, J. Kamalakkannan, S. Prabha, and S. Senthilvelan, "Sol-gel synthesis of TiO_2 /SiO_2 and ZnO/SiO_2 composite films and evaluation of their photocatalytic activity towards methyl green," *Journal of Nanoparticles*, vol. 2013, Article ID 507161, 7 pages, 2013.

[73] K. S. Al-Namshah, S. M. Mariappan, M. Shkir, and M. S. Hamdy, "Photocatalytic degradation mechanism of Ce-loaded ZnO catalysts toward methyl green dye pollutant," *Applied Physics A*, vol. 127, no. 6, pp. 1–10, 2021.

[74] H. B. Hadjltaief, A. Omri, M. B. Zina, P. Da Costa, and M. E. Galvez, "Titanium dioxide supported on different porous materials as photocatalyst for the degradation of methyl green in wastewaters," *Advances in Materials Science and Engineering*, vol. 2015, Article ID 759853, 10 pages, 2015.

[75] X. Ren, Z. Hu, H. Hu et al., "Noncovalently-functionalized reduced graphene oxide sheets by water-soluble methyl green for supercapacitor application," *Materials Research Bulletin*, vol. 70, pp. 215–221, 2015.

[76] I. L. da Silva Santana, A. A. Barbosa, M. G. Silva et al., "Titanium dioxide immobilization in recycled aluminum net for degradation of textile dye by heterogeneous photocatalysis trough neural networks," *Revista Eletrônica em Gestão, Educação e Tecnologia Ambiental*, vol. 23, p. 27, 2019.

[77] K. A. Isai and V. S. Shrivastava, "Photocatalytic degradation of methylene blue using ZnO and 2% Fe–ZnO semiconductor nanomaterials synthesized by sol–gel method: a comparative study," *SN Applied Sciences*, vol. 1, no. 10, pp. 1–11, 2019.

[78] A. Kumar and G. Pandey, "The photocatalytic degradation of methyl green in presence of visible light with photoactive $Ni_{0.10}$: $La_{0.05}$: TiO_2 nanocomposites," *IOSR-JAC*, vol. 10, no. 9, pp. 31–44, 2017.

[79] N. M. Mahmoodi, U. Sadeghi, A. Maleki, B. Hayati, and F. Najafi, "Synthesis of cationic polymeric adsorbent and dye removal isotherm, kinetic and thermodynamic," *Journal of Industrial and Engineering Chemistry*, vol. 20, no. 5, pp. 2745–2753, 2014.

[80] W. Li, G. Wang, C. Chen, J. Liao, and Z. Li, "Enhanced visible light photocatalytic activity of ZnO nanowires doped with Mn^{2+} and Co^{2+} ions," *Nanomaterials*, vol. 7, no. 1, p. 20, 2017.

[81] M. Nirmala, M. G. Nair, K. Rekha, A. Anukaliani, S. Samdarshi, and R. G. Nair, "Photocatalytic activity of ZnO nanopowders synthesized by DC thermal plasma," *African Journal of Basic & Applied Sciences*, vol. 2, no. 5-6, pp. 161–166, 2010.

[82] L. Anju Chanu, W. Joychandra Singh, K. Jugeshwar Singh, and K. Nomita Devi, "Effect of operational parameters on the photocatalytic degradation of methylene blue dye solution using manganese doped ZnO nanoparticles," *Results in Physics*, vol. 12, pp. 1230–1237, 2019.

[83] M. B. Ibanescu, V. Musat, T. Textor, and B. Mahltig, "Functional finishing of textile using manganese doped zinc oxide based coatings obtained by sol-gel method," *Revista de Chimie*, vol. 65, no. 6, pp. 689–693, 2014.

[84] J. Gupta, P. Hassan, and K. Barick, "Structural, photoluminescence, and photocatalytic properties of Mn and Eu co-doped ZnO nanoparticles," *Materials Today: Proceedings*, vol. 42, pp. 926–931, 2021.

[85] C. B. Ong, L. Y. Ng, and A. W. Mohammad, "A review of ZnO nanoparticles as solar photocatalysts: synthesis, mechanisms and applications," *Renewable and Sustainable Energy Reviews*, vol. 81, pp. 536–551, 2018.

[86] K. Qi, B. Cheng, J. Yu, and W. Ho, "Review on the improvement of the photocatalytic and antibacterial activities of ZnO," *Journal of Alloys and Compounds*, vol. 727, pp. 792–820, 2017.

[87] K. M. Lee, C. W. Lai, K. S. Ngai, and J. C. Juan, "Recent developments of zinc oxide based photocatalyst in water treatment technology: a review," *Water Research*, vol. 88, pp. 428–448, 2016.

[88] Y. Wang, Q. Wang, X. Zhan, F. Wang, M. Safdar, and J. He, "Visible light driven type II heterostructures and their enhanced photocatalysis properties: a review," *Nanoscale*, vol. 5, no. 18, pp. 8326–8339, 2013.

[89] K. Lefatshe, G. T. Mola, and C. M. Muiva, "Reduction of hazardous reactive oxygen species (ROS) production of ZnO through Mn inclusion for possible UV-radiation shielding application," *Heliyon*, vol. 6, no. 6, article e04186, 2020.

[90] M. A. M. Adnan, N. M. Julkapli, and S. B. A. Hamid, "Review on ZnO hybrid photocatalyst: impact on photocatalytic activities of water pollutant degradation," *Reviews in Inorganic Chemistry*, vol. 36, no. 2, pp. 77–104, 2016.

[91] S. B. Satpal and A. A. Athawale, "Synthesis of ZnO and Nd doped ZnO polyscales for removal of rhodamine 6G dye under UV light irradiation," *Materials Research Express*, vol. 5, no. 8, article 085501, 2018.

[92] K. N. Devi, S. A. Devi, W. J. Singh, and K. J. Singh, "Nickel doped zinc oxide with improved photocatalytic activity for malachite green dye degradation and parameters affecting the degradation," *Journal of Materials Science: Materials in Electronics*, vol. 32, no. 7, pp. 8733–8745, 2021.

[93] A. Nezamzadeh-Ejhieh and Z. Shams-Ghahfarokhi, "Photodegradation of methyl green by nickel-dimethylglyoxime/ZSM-5 zeolite as a heterogeneous catalyst," *Journal of Chemistry*, vol. 2013, Article ID 104093, 11 pages, 2013.

[94] K. V. Chandekar, M. Shkir, B. M. al-Shehri et al., "Visible light sensitive Cu doped ZnO: facile synthesis, characterization and high photocatalytic response," *Materials Characterization*, vol. 165, article 110387, 2020.

[95] M. Shkir, K. V. Chandekar, B. M. Alshehri, A. Khan, S. AlFaify, and M. S. Hamdy, "A remarkable enhancement in photocatalytic activity of facilely synthesized terbium@zinc oxide nanoparticles by flash combustion route for optoelectronic applications," *Applied Nanoscience*, vol. 10, no. 6, pp. 1811–1823, 2020.